Insights into durable NiCo catalysts on β-SiC/CeZrO$_2$ and γ-Al$_2$O$_3$/CeZrO$_2$ advanced supports prepared from facile methods for CH$_4$–CO$_2$ dry reforming

Moom Sinn Aw [a,*], Milena Zorko [b], Petar Djinović [a], Albin Pintar [a,c]

[a] *Laboratory for Environmental Sciences and Engineering, National Institute of Chemistry, Hajdrihova 19, SI-1001 Ljubljana, Slovenia*
[b] *Laboratory for Materials Chemistry, National Institute of Chemistry, Hajdrihova 19, SI-1001, Ljubljana, Slovenia*
[c] *Centre of Excellence "Low Carbon Technologies", Hajdrihova 19, SI-1001 Ljubljana, Slovenia*

ARTICLE INFO

ABSTRACT

This study explores CeZrO$_2$ deposited over commercial β-SiC, and a highly ordered 3D β-SiC synthesised in the laboratory *via* electrophoretic deposition, as well as γ-Al$_2$O$_3$ in order to prepare three types of dual support for NiCo bimetallic catalyst in CH$_4$–CO$_2$ dry reforming (DR). CeZrO$_2$ was deposited over γ-Al$_2$O$_3$ and β-SiC by dry impregnation (DI), wet impregnation (WI) and 2-step deposition precipitation (DP). XRD analysis indicated that the constituents of the dual supports were retained after calcination, as well as before and after the DR reaction. CeZrO$_2$ remained as a mixed oxide solid solution, whilst alumina formed spinel structures with Ni and Co before the catalysts were reduced in H$_2$ during the pretreatment step prior to the activity tests. During 550 h stability tests, WI, 2-step SICAT/CeZrO$_2$ and 2-step γ-Al$_2$O$_3$/CeZrO$_2$ solids were identified as the most promising catalysts, maintaining high DR activities without deactivation. Notably, 2-step SiC(SICAT) and 2-step γ-Al$_2$O$_3$/CeZrO$_2$ samples recorded the highest yield (H$_2$ = 77%, CO = 90%; H$_2$ = 71%, CO = 81%), with a coke content of 7.7 and 0.6 wt.%, respectively. Carbon deposition for the former is high; contrarily, for WI SiC(SICAT) solid, it accumulated a lower amount of 2.6 wt.%. No agglomeration of CeZrO$_2$ and NiCo phases was observed, evidencing excellent robustness and thermal resistance of these dual supports.

© 2014 Elsevier B.V. All rights reserved.

1. Introduction

In order to reduce our dependence on the diminishing fossil fuel reserves and to achieve resourcefulness in renewable energy, methane–carbon dioxide (CH$_4$–CO$_2$) dry reforming (DR) reaction has been of growing interest in the study of heterogeneous catalysis. This process holds much incentive in exploiting CH$_4$ and CO$_2$ (two major pollutants in air which cause the greenhouse effects) as reactants for their conversion into syngas. These two carbon-containing gases can be produced efficiently on a large scale by anaerobic digestion of organic substrates in a fully renewable and sustainable manner. Syngas is immensely valuable for downstream processes, such as the Fischer–Tropsch synthesis [1], hydrocarbon hydrogenation for fuel production and the synthesis of oxygenates [2]. Methane reforming with carbon dioxide (reaction (1)) could

provide an alternative for producing renewable syngas with simultaneous possibility of converting potent greenhouse gases into useful platform chemicals:

$$CH_4 + CO_2 \leftrightarrow 2H_2 + 2CO; \Delta H^\circ{}_{298\,K} = +247\,kJ/mol \tag{1}$$
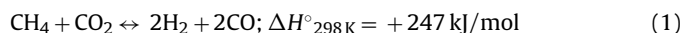
Although catalyst preparation has reached extraordinary levels of sophistication in recent years, the development of practical and efficient methodologies still requires improvements to generate cleaner and simpler synthesis technology feasible for upscaling and for catalyst syntheses in actual industrial processes. Thus far, amongst all that were tested for CH$_4$–CO$_2$ DR, nickel (Ni) and cobalt (Co) are two of the most active and economically viable catalysts. However, Ni is susceptible to coking, whilst Co has a high tendency to oxidise, altogether obstructing their implementation for long-term industrial applications [3,4]. A possible solution to resolve these problems includes the incorporation of a support with high oxygen storage capacity (OSC), such as ceria to scavenge carbon deposits, and zirconia with outstanding thermal stability and mechanical strength to compensate for the thermal and structural sensitivity of ceria [5]. Ceria is also considered a versatile

* Corresponding author. Tel.: +386 1 47 60 249; fax: +386 1 47 60 460.
E-mail addresses: moom.sinn.aw@ki.si, awymy001@mymail.unisa.edu.au (M.S. Aw).

support due to its amphoteric character [6]. In the course of devising advanced supports for NiCo bimetallic catalyst in CH_4–CO_2 DR, there exists constraints in support candidates such as alumina, in which heat transfer was reported to be poor [7], whereas for carbon and silica, their lack of anchoring surface functional groups was found to reduce the surface area of active metal phases [8]. Since the behaviour of active phases is strongly influenced by the type of support material, it is compulsory to select an optimum support material based on the criteria of inertness, textural properties, stability, support interaction with active phases and acceptable cost at the commercial scale [9,10]. In particular, recent literature underlines the significance of diverse functionality in a working catalyst for CH_4–CO_2 DR [11]. Hence, the aim of this work is to advance the synthesis of a support by complementing the advantage of each component to render synergistic properties in a hybrid composite comprised of a novel dual support instead. We devise a strategy incorporating ceria–zirconia ($CeZrO_2$) and either gamma alumina (γ-Al_2O_3), or silicon carbide (β-SiC) as dual supports to anchor NiCo metal particles, with the aim of combining the advantages of $CeZrO_2$, such as high surface area, high redox properties as well as the high corrosion/hydrothermal/oxidation resistance and the controlled porosity of β-SiC [12], or high chemical/thermal stability, porosity and surface area of γ-Al_2O_3 [13]—in a joint effort to enhance the CH_4–CO_2 DR performance. SiC with its high thermal conductivity, hardness [14], resistance to wear and fracture, specific stiffness [15], and γ-Al_2O_3 with its advantages such as high specific surface area (up to $300\,m^2/g$), outstanding mechanical properties, compatible nature of interaction with active phases, controllable surface acidity and high thermal stability, were selected in our work, since they are amongst the most abundantly applied commercial catalyst supports suitable for mass production. β-SiC is an attractive support material by virtue of its tuneable morphology (to form different shapes, *i.e.* monoliths, pellets, foams, extrudates and honeycomb), easy obtainability, inertness, feasible manufacturing and the ability to withstand extreme temperatures and pressures [16]. Its high thermal conductivity can also improve heat transfer within the catalyst bed during the highly endothermic DR reaction to generate a more homogeneous temperature profile [17]. In addition to that, it has no known adverse effects on the environment.

This work, which is an extension of our previous studies [18–20], showcases for the first time, 3 wt.% Ni and Co metals anchored on a dual support, which consists of three types of composite materials: (i) $CeZrO_2$ and γ-Al_2O_3; (ii) $CeZrO_2$ and β-SiC synthesised *via* electrophoresis in our laboratory; (iii) $CeZrO_2$ and β-SiC (obtained from SICAT). Since preparative procedures impose considerable influence on the catalyst structure [21], several approaches were used, namely, wet (WI) and dry impregnation (DI), alongside 2-step deposition precipitation (DP) to prepare these dual supports. Structural characterisation and activity tests for 20 and 550 h (*i.e.* short- and long-term DR) were conducted on these supported catalysts. Their properties were then correlated to the activity tests and compared in detail.

2. Experimental

2.1. Synthesis of dual supports

Ceria–zirconia ($Ce_xZr_{1-x}O_2$, denoted as $CeZrO_2$) with a wt. ratio set at ce:Zr = 4:1 was prepared glycothermally with ethylene glycol ($C_2H_6O_2$, EG). 1 g of $Ce(NO_3)_3 \cdot 6H_2O$ ($Mw = 434\,g/mol$; Fluka, p.a.) and $ZrO(NO_3)_2 \cdot 5.82H_2O$ ($Mw = 336\,g/mol$; Sigma Aldrich, >99% purity) were used as nitrate precursors. Precisely, 0.787 g of $Ce(NO_3)_3 \cdot 6H_2O$ and 0.213 g of $ZrO(NO_3)_2 \cdot 5.82H_2O$ were prepared. They were dissolved in 1 mL Milli-Q water, 1 mL propanoic acid

(C_2H_5COOH) (Merck, >99% purity) and 15 mL EG (Merck, >99% purity). The mixture was aged at 180 °C for 200 min in Teflon-clad stainless steel autoclaves, before solids in the esterified suspension were separated by centrifugation at 9000 rpm in 15 min cycles. The obtained solids were washed with Milli-Q water and ethanol (absolute, ≥99.8%, Sigma-Aldrich), followed by 24 h oven-drying at 100 °C and 4 h calcination at 350 °C, with a final grinding step in the mortar to obtain fine powdered form of $CeZrO_2$ [22].

To synthesise the three types of dual support, $CeZrO_2$ material was deposited over either commercially procured γ-Al_2O_3 (Nikki-Universal Co., Tokyo, Japan) or β-SiC. Two types of SiC were used. The first was β-SiC obtained from SICAT (SICAT Catalysts Inc., Willstätt, Germany) manufactured through SICAT's proprietary self-bonding SiC process, whereas the second was 3D mesoporous β-SiC with highly ordered porosity prepared *via* electrophoretic deposition. Preparation steps for both processes were explained in detail in Supplementary data (Section S1.1 and Section S1.2). The combination of $CeZrO_2$ with γ-Al_2O_3, SiC(lab) or SiC(SICAT), with a wt. ratio of 1: 1, was carried out *via* 2-step deposition precipitation (DP). The protocol for the 2-step DP was elaborated in detail in Supplementary data (Section S1.3). The other two methods employed were: dry (DI) and wet impregnation (WI), whereby $Ce(NO_3)_3 \cdot 6H_2O$ and $ZrO(NO_3)_2 \cdot 5.82H_2O$ as the nitrate precursors for $CeZrO_2$ were impregnated onto the γ-Al_2O_3 or β-SiC powder in an aqueous solution. The suspensions were dried at 100 °C overnight and calcined at 300 °C (for β-SiC) or 800 °C (for γ-Al_2O_3), both at a heating ramp of 2 °C/min for 4 h from the start at room temperature (RT) until the final calcination temperature was achieved.

2.1.1. Anchoring of NiCo active phase

The loading of 3 wt.% NiCo metal solids with a wt. ratio of Ni:Co = 2:3 onto the various supports, *i.e.* $CeZrO_2$:γ-Al_2O_3, $CeZrO_2$:SiC(lab) and $CeZrO_2$:SiC(SICAT) with the dual support wt. ratio = 1:1, was performed *via* deposition precipitation (DP) through the hydrolysis of 0.3 M urea under reflux at 90 °C for 22 h (similar to the previously mentioned 2-step DP). The metal solids were filtered, washed copiously with water and absolute ethanol before being dried in the oven overnight at 70 °C and calcined at 650 °C for 4 h. To this end, the as-synthesised catalysts are abbreviated as follows: 3 wt.% NiCo/DI or WI or 2-step γ-Al_2O_3–$CeZrO_2$, 3 wt.% NiCo/DI or WI or 2-step SiC(lab)–$CeZrO_2$, 3 wt.% NiCo/DI or WI or 2-step SiC(SICAT)–$CeZrO_2$.

2.2. Characterisation of supported catalysts

2.2.1. X-ray powder diffraction (XRD)

The crystalline phases of the supports only (single supports), calcined fresh catalysts and spent catalysts were characterised using a X'pert Pro by PANalytical X-ray diffractometer (XRD) with Cu$K\alpha_1$ non-monochromatic radiation ($\lambda = 1.5406\,Å$). The intensity was measured by stepwise scanning in the 2θ range of 5 to 90°. The x-ray diffractograms were recorded at an acquisition time of 100 s per step with an increment of 0.034°. The identification of the phases and diffraction lines was performed using the reference data from JCPDS files. Mean crystallite sizes of the supported catalysts were calculated from line broadening of the most intense reflection using the Scherrer's equation. X-ray powder diffractometer PANalytical X'Pert PRO HTK was used to measure the reduced fresh catalysts after activation in H_2 for 1 h at 750 °C (same pretreatment conditions for all catalysts prior to DR reaction) in an X-ray reactor chamber, whereby the XRD patterns were recorded *in situ* at the reductive atmosphere at high temperatures.

2.2.2. Textural characteristics

Textural characteristics of (i) the support only ((a) single, (b) dual), (ii) supported fresh and (iii) spent catalysts were evaluated by means of N_2 sorption using a Micromeritics Tristar II 3020 apparatus. Prior to measurements, samples were degassed in N_2 flow for 1 h at 90 °C, followed by 4 h thermal heating at 180 °C in the Micromeritics SmartPrep Degasser. The specific surface areas were determined by the multi-point BET method. Pore width and pore volume data are reported together with the BET surface area, in which the pore volume was calculated from the amount of N_2 adsorbed at a relative pressure P/P_0 of 0.99. Pore size distribution curves were determined from the desorption branch of the isotherms using the model proposed by Barrett, Joyner and Halenda (BJH).

2.2.3. UV–Vis diffuse reflectance spectroscopy (UV–Vis DRS)

UV–Vis diffuse reflectance spectra in the range of 200 to 900 nm were recorded on a computer controlled, double beam Lambda 35 UV–Vis spectrophotometer (Perkin Elmer) equipped with the RSA-PE-19 M Praying Mantis accessory, which is designed for diffuse reflectance measurements of horizontally positioned powdered samples. Before measurements were conducted for the catalysts (all in powdered form), the white reflectance standard Spectralon® was used as the blank (reference) sample to perform the instrument baseline correction, with conditions of spectra acquisition as the following ordinate mode: absorbance, slit width: 4 nm, scan speed: 120 nm/min.

2.2.4. Raman spectroscopy

Dispersive Raman spectrometer (Renishaw inVia Raman microscope) with a laser beam measuring at 532 nm and a spectrum bandwidth range of 120 to 4500 cm^{-1} was used on several chosen samples of interest, i.e. fresh and spent catalysts supported on 2-step prepared γ-Al$_2$O$_3$– and SiC(SICAT)–CeZrO$_2$ to observe any given vibrational, rotational and other low-frequency modes of chemical bonds in the compound structure.

2.2.5. Temperature-programmed reduction with hydrogen (TPR-H_2)

TPR-H_2 analysis was performed using the Pyris 1 TGA instrument (Perkin Elmer). About 15 mg of sample was mounted in a platinum pan before it was loaded in the furnace. For pre-treatment, all catalysts were heated from RT to 300 °C to be degassed in situ under N_2 gas flow at 50 N mL/min. This temperature was held for 1 h during an isothermal step. The temperature was later cooled down to 50 °C and stabilised for 15 min. TPR-H_2 was carried out in a 4.5 v/v % H_2/N_2 gas atmosphere at a flow rate of 115 N mL/min. The temperature was ramped at 10 °C/min from 50 to 900 °C, followed by a 10 min isothermal step. Weight loss as well as the derivative weight loss data were recorded, and their graphs were plotted against time for determining the reducibility of the support and the supported catalysts.

2.2.6. CO pulse chemisorption

The CO pulse chemisorption measurements were performed for several chosen catalysts that are promising, based on acquired results from other characterisation techniques and the DR tests, using the Micromeritics AutoChem II 2920 apparatus. First, each sample was weighed to 100 mg, and then inserted into a U-shaped quartz reactor tube laid on top of a flock of quartz wool. The sample was reduced under a flow of 5 vol.% H_2/Ar from RT to 750 °C. After cooling to 30 °C at a ramp of 10 °C/min under a flow of He, pulses of CO (5 vol.% in He; loop volume of 0.5324 mL at STP) were injected into the He stream passing through the reactor. The CO gas injection was programmed to be repeated until the final peak was equal to

the penultimate one before it was stopped. NiCo dispersion was calculated based on the amount of consumed CO using the integrated Peak Editor software, with an average relative error of less than 3%. Spherical shaped NiCo clusters were assumed along with a 1:1 stoichiometric ratio for CO molecule chemisorption onto each surfaced Ni or Co atom. The CeZrO$_2$/Al$_2$O$_3$ or CeZrO$_2$/SiC dual supports were used as blanks in separate measurements. Obtained values with NiCo/CeZrO$_2$–Al$_2$O$_3$ or NiCo/CeZrO$_2$–SiC were then corrected for the contribution from CO adsorption on ceria.

2.2.7. CH$_4$–CO$_2$ dry reforming (DR) activity test

Catalysts were placed in a fixed bed comprised of 0.5 g well-mixed catalyst powder diluted with 2.8 g of SiC sand (grain size = 200–500 μm). Temperature was measured using a K-type thermocouple that was positioned at the centre of the bed. Each bed was sandwiched between two flocks of quartz wool in a vertical quartz tubular reactor (I.D. = 10 mm) in the Microactivity Reference reactor system manufactured by PID Eng&Tech. The catalysts were reduced in situ in a 50 N mL/min flow of 20% H_2/N_2 by heating them from RT to 750 °C at a ramp of 10 °C/min. This was followed by an isothermal step at 750 °C for 1 h to ensure their full transformation into metallic phase. CH$_4$–CO$_2$ DR activity tests were run at the same temperature and an absolute operating pressure of 1.2 bar for 20 h under undiluted, equimolar flow of CH$_4$/CO$_2$, each at 50 N mL/min, simulating real conditions (WHSV = 12 L/(g_{cat} h)). Reactor effluents were fed through a heated capillary (I.D. = 0.16 cm at 200 °C) to the GC (Agilent Technologies, model 7890A), where quantitative and qualitative composition of the gases was determined. Long-term stability tests of 550 h were performed for a selected few of the promising catalysts. Lastly, an ~80 h long catalytic run with non-equimolar ratio of CH$_4$: CO$_2$ = 60: 40 i.e. 60 N mL/min for CH$_4$ and 40 N mL/min CO$_2$ (undiluted) was carried out for NiCo/WI CeZrO$_2$–SiC(SICAT) to confirm its long-term stability under harsh conditions.

2.2.8. Scanning electron microscopy (SEM) and energy dispersive X-ray spectroscopy (EDXS)

Surface morphology of the supported catalysts (fresh and spent) was analysed using Supra 35 VP field emission scanning electron microscope (Carl Zeiss). The energy dispersive X-ray analysis (EDX) hardware (Oxford Instruments) that the microscope is equipped with was used to analyse the elemental compositions of these samples.

2.2.9. Temperature-programmed oxidation (TPO) and CHNS elemental analyses

The extent of coking after DR reactions for both the short-term (20 h) and long-term (550 h) tests was evaluated through the amount of carbon formed on the spent catalysts, which was determined by TPO analysis using STA 6000 apparatus (Perkin Elmer). This was carried out in air by heating them from RT to 900 °C and quantifying the difference between the initial and final mass. CHNS elemental analysis (Perkin Elmer, model 2400 Series II) was also performed to validate the results.

3. Results and discussion

3.1. XRD analysis

3.1.1. XRD of fresh and calcined catalysts

Fig. 1 displays XRD diffractograms for (a) 3 wt.% NiCo/CeZrO$_2$–γ-Al$_2$O$_3$, (b) 3 wt.% NiCo/CeZrO$_2$–SiC(lab), and (c) 3 wt.% NiCo/CeZrO$_2$–SiC(SICAT) fresh, calcined samples prepared by means of 2-step DP, dry (DI) and wet (WI) impregnation. The peaks can be assigned to their respective compounds as shown in the colour-coded legends, for instance, in Fig. 1a, viz. Ce$_{0.75}$Zr$_{0.25}$O$_2$,
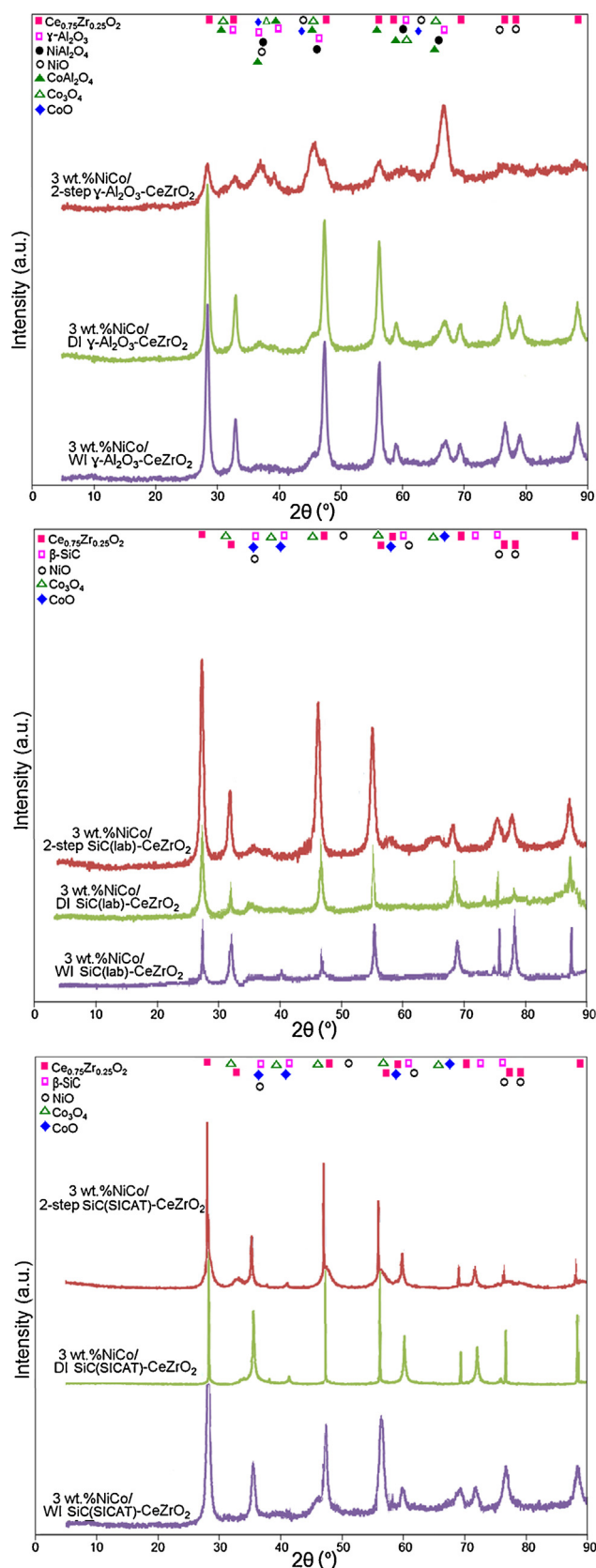
Fig. 1. XRD data for the fresh catalysts (obtained after calcination) (a) 3 wt.% NiCo/CeZrO$_2$–γ-Al$_2$O$_3$, (b) 3 wt.% NiCo/CeZrO$_2$–SiC(lab) and (c) 3 wt.% NiCo/CeZrO$_2$–SiC(SICAT), with the dual support prepared by 2-step deposition precipitation (DP), wet (WI) and dry impregnation (DI) methods.

γ-Al$_2$O$_3$, NiAl$_2$O$_4$, NiO, CoAl$_2$O$_4$, Co$_3$O$_4$ and CoO. The characteristic peaks at 28.87, 33.47, 48.05 and 57.01° can be assigned to the fluorite structure of Ce$_{0.75}$Zr$_{0.25}$O$_2$ solid solution (JCPDS PDF 028-0271) [19]. The presence of CeZrO$_2$ is more pronounced for DI and WI samples, *i.e.* larger and more crystalline CeZrO$_2$ phase was formed. Contrarily, diffraction peaks of γ-Al$_2$O$_3$ are narrower, more intense in the 2-step DP sample, possibly as a result of two consecutive DP steps, which could induce morphological changes in the support material. Based on JCPDS PDF 29-0063, peaks at 31.7, 37.8, 45.7, 60.8 and 66.9° were assigned to reflections from (2 2 0), (3 1 1), (4 0 0), (5 1 1) and (4 4 0) planes of γ-Al$_2$O$_3$ [23], which comprises a defect cubic spinel lattice. The higher crystallinity of γ-Al$_2$O$_3$ in these samples likely originates from partial dissolution and re-precipitation in the highly acidic medium (pH < 3), as was present during the impregnation with nitrate precursors of ceria and zirconia. Because of the high grain boundary density of γ-Al$_2$O$_3$, its defect spinel structure and its thermodynamic metastability, γ-Al$_2$O$_3$ could react with Ni and Co *via* diffusion of these atoms into the bulk support, possibly contributing to the formation of spinel phases. NiAl$_2$O$_4$ and CoAl$_2$O$_4$ spinels could be formed as these are defect cubic spinel structures with vacancies on the Al^{3+} positions [24]. The presence of NiAl$_2$O$_4$ can be assigned to several peaks emerging at 2θ = 37.1, 45.3 and 59.7° [25]. However, the presence of CoAl$_2$O$_4$ cannot be established unequivocally by means of XRD. This is due to the fact that the CoAl$_2$O$_4$ diffraction peaks have almost the same positions as the rather broad γ-Al$_2$O$_3$ peaks [26]. It is also difficult to distinguish between NiAl$_2$O$_4$ and γ-Al$_2$O$_3$, and CoAl$_2$O$_4$ with Co$_3$O$_4$, because these diffraction peaks were superimposed on one another. Based on JCPDS PDF 10-458, the formation of CoO and CoAl$_2$O$_4$ can be identified from separate characteristic peaks as shown in Fig. 1a [27]. However, since CoAl$_2$O$_4$ spinel and Co$_3$O$_4$ display characteristic diffraction peaks at the same positions [28], the presence or absence of Co$_3$O$_4$ cannot be distinguished by this technique. A small shoulder peak at 43.7° corresponds to the reflection from the (2 0 0) crystalline plane of NiO in the DI and WI samples [29,30]. In order to verify the existence of NiAl$_2$O$_4$ and CoAl$_2$O$_4$ spinels, UV–Vis diffuse reflectance spectroscopy was employed as another technique to characterise these catalysts (Fig. 3).

For SiC(lab)-based samples, the most pronounced peak was observed at 28.8°. This peak was shifted to higher 2θ values from the corresponding (1 1 1) plane of ceria that is originally located at 28.55° (JCPDS PDF 34-0394). The peak belonging to β-SiC was detected at 59.9° that is part of the broad peak, overlapping with reflections of CeZrO$_2$, NiO and CoO phases. For the 2-step catalyst, it corresponds to (2 2 0) plane of β-SiC, which is assigned to a minor peak [31]. The intensity of the peaks for CeZrO$_2$ introduced *via* the DI and WI methods decreased remarkably from the 2-step DP preparation steps, indicating larger particles in the latter catalysts. For SiC(SICAT)-based samples, no ordered zirconia phase was detected in the XRD diffractograms, implying no presence of separate, segregated phase, and that Zr was incorporated within the ceria structure to form Ce$_{0.75}$Zr$_{0.25}$O$_2$ solid solution instead. In other words, ceria–zirconia solid solution is seen in all the fresh catalysts. Similarly for Fig. 1a and b, peaks characteristic for this solid solution also emerged in Fig. 1c. Specifically, 28.6, 33.1, 47.5, 56.3, 59.1, 69.4, 76.7, 79.1 and 88.4° can be assigned to ceria planes of (1 1 1), (2 0 0), (2 2 0), (3 1 1), (2 2 2), (4 0 0), (3 3 1), (4 2 0) and (4 2 2), albeit slight shifting in the diffractograms. Nevertheless, peaks belonging to β-SiC at 35.6, 41.3 and 60.0° were seen in Fig. 1c, corresponding to its (111), (200) and (220) planes [32]. These belong to the cubic crystallographic structure with $F43m(316)$ space group for the β-SiC supported catalysts. All peaks, in fact, are much sharper than the ones in Fig. 1b, indicating larger crystallite sizes of SiC(SICAT) than SiC(lab). This can be further substantiated by comparing the BET surface areas of both SiC materials, as the one prepared in our

Table 1
Textural properties of single and dual supports after calcination, and as-synthesised 3 wt.% NiCo catalysts anchored on dual supports (CeZrO$_2$–γ-Al$_2$O$_3$ and CeZrO$_2$–SiC).

Sample	S_{BET} (m^2/g)	V_{pore} (cm^3/g)	d_{pore} (nm)	$\rho_{skeletal}$ (g/cm^3)
Supports				
CeZrO$_2$	158	0.22	5.6	5.39
γ-Al$_2$O$_3$	170	0.83	17.8	3.24
SiC(lab)	295	0.44	5.8	2.05
SiC(SICAT)	18.0	0.09	18.8	2.91
γ-Al$_2$O$_3$–CeZrO$_2$	165	0.67	13.2	4.56
SiC(lab)–CeZrO$_2$	189	0.34	5.7	4.16
SiC(SICAT)–CeZrO$_2$	77.2	0.15	12.4	4.44
Fresh catalysts				
2-Step γ-Al$_2$O$_3$–CeZrO$_2$	117	0.55	19.1	4.72
DI γ-Al$_2$O$_3$–CeZrO$_2$	83.0	0.44	20.5	3.53
WI γ-Al$_2$O$_3$–CeZrO$_2$	86.5	0.46	17.2	4.00
2-Step SiC (lab)–CeZrO$_2$	158	0.22	5.6	3.62
DI SiC (lab)–CeZrO$_2$	130	0.20	5.9	4.55
WI SiC (lab)–CeZrO$_2$	173	0.34	5.0	3.00
2-Step SiC (SICAT)–CeZrO$_2$	58.0	0.12	8.1	3.87
DI SiC (SICAT)–CeZrO$_2$	38.0	0.12	11.0	2.94
WI SiC (SICAT)–CeZrO$_2$	38.2	0.08	7.2	3.74

laboratory is approximately 20 times higher than the tested commercial one (Table 1).

3.1.2. Crystallite size of powdered samples

For the mean crystallite size of the samples, the values were tabulated in Table 2. They were calculated from full-width at half maximum (FWHM) of the most prominent XRD peaks by the Scherrer's equation. As previously seen in Fig. 1 that displays XRD diffractograms of the CeZrO$_2$ solid solutions, they resemble those of ceria, but shifted to higher 2θ values, similar to solid solutions prepared from other methods such as high energy ball milling and co-precipitation [33], all of which reported the same behaviour attributed to the insertion of zirconium ions of smaller radii into the cubic matrices of ceria, resulting in the contraction of the lattice. Crystallite size is the smallest for SiC(lab)-based catalyst (7.6 nm), followed by γ-Al$_2$O$_3$ (11.5 nm), and lastly SiC(SICAT) (11 nm). The 2-step method, on average, resulted in smaller crystallites than DI and WI, which is also in agreement with the XRD diffraction spectra.

3.1.3. XRD for supports, reduced and spent catalysts

The XRD spectra for calcined fresh support without metal deposits, reduced dual supports and fresh catalysts, as well as the spent catalysts after the 20 h DR reaction were shown in Fig. 2.

In Fig. 2a, the strong broad peaks at 37, 46 and 66° are ascribed to the diffraction of the alumina support. In Fig. 2b, It is noticed that peaks belonging to Ni and Co metals can be seen for the reduced fresh catalysts NiCo/WI CeZrO$_2$-γ-Al$_2$O$_3$ and NiCo/WI CeZrO$_2$-SiC(SICAT). Peaks at 45.5 and 78.3° are detected for the γ-Al$_2$O$_3$-based reduced catalyst, indicating the presence of Ni metallic structure with a cubic form containing the *Fm*3*m* space group [34]. The peak at 45.5° is also detected for Ni^0 in the reduced catalyst NiCo/WI CeZrO$_2$–SiC(SICAT). Moreover, the peaks at 41.6, 44.3, 47.4 and 75.9° for this sample can be assigned to Co with a hexagonal crystalline structure and the *p*63/*mmc* space group. Three of these signals (44.3, 47.4 and 75.9°) can also be seen for the γ-Al$_2$O$_3$-based reduced catalyst [35]. Notably, peaks belonging to the NiAl$_2$O$_4$ and CoAl$_2$O$_4$ spinels were no longer detected. This indicates that the NiAl$_2$O$_4$ and CoAl$_2$O$_4$ spinels, NiO and Co$_3$O$_4$ particles that were present before in the calcined fresh samples have been reduced to active metal phases after the same activation conditions were employed for the reduction of catalysts prior to the DR reactions [36,37]. In Fig. 2c, peaks that otherwise did not appear in Fig. 2b for the reduced fresh samples, which correspond to NiO and Co$_3$O$_4$ can be seen, *i.e.* the peak at 37.3° for NiO can be observed for spent NiCo/2-step CeZrO$_2$-γ-Al$_2$O$_3$ and spent NiCo/2-step CeZrO$_2$–SiC(SICAT) [38], whereas diffraction peaks characteristics of the Co$_3$O$_4$ cubic spinel structure can be detected for the spent samples NiCo/WI CeZrO$_2$-γ-Al$_2$O$_3$ and NiCo/WI CeZrO$_2$–SiC(SICAT).

To summarise, no peaks can be accounted for crystalline Ni and/or Co metals on the fresh, calcined γ-Al$_2$O$_3$ and SiC catalysts in Fig. 1a–c. The presence of Ni and/or Co metals for such low loadings and in the presence of CeZrO$_2$ is unlikely to be detected, which is also possible due to their high dispersion on the support. It is suggested that they are well dispersed on the dual supports and were not detected due to their oxidised form before they were reduced in H$_2$. Contrarily, their peaks that correspond to the active metallic phases can be observed in the reduced samples as shown in Fig. 2b, implying that the transformation from the initial oxidised and spinel states has occurred. Nevertheless, they were re-oxidised after the DR reactions as shown in the spent samples (Fig. 2c).

3.2. Textural properties of dual supports and supported catalysts

Table 1 depicts the BET surface area, pore volume, pore width and skeletal density for each of the single and dual supports, including the textural properties for the NiCo-loaded catalysts. It can be seen that SiC(lab) recorded the highest BET surface area (295 m^2/g), followed by γ-Al$_2$O$_3$ (170 m^2/g), then CeZrO$_2$ (158 m^2/g), and lastly SiC(SICAT) (18 m^2/g). The high surface area of SiC(lab) is ascribed to its highly ordered 3D structure derived from silica nanospheres used as its initial template, prepared by means of the Stöber–Fink–Bohn approach [39]. The extremely thin walls that are several nm thick also gave rise to greater dimensional exposure and surface area. It is a highly favourable trait, as pore surface of the support plays an important role to disperse the active metal for efficient exposure to and contact with the gaseous reactants. As aforementioned, its surface area is more than an order of magnitude larger than SiC(SICAT). As for the pore volume of the support, it is equally important during the preparation steps as well as the reaction *per se*. For the single support, pore volume is the greatest in γ-Al$_2$O$_3$ (0.83 cm^3/g), followed by SiC(lab) (0.44 cm^3/g), CeZrO$_2$ (0.22 cm^3/g), and lastly SiC(SICAT) (0.09 cm^3/g). γ-Al$_2$O$_3$, being the most porous, can accommodate the highest amount of CeZrO$_2$ in its pores, as confirmed by comparing the total pore volumes before and after the deposition. In comparison to literature, our γ-Al$_2$O$_3$ has similar BET surface area to other groups, but higher pore volume (0.83 > 0.29–0.47 cm^3/g) and higher pore width (17.8 > 3.8–6.8 nm) [40,41]. Although high surface area is advantageous, a portion was unfortunately lost during subsequent steps of the dual support preparation. This occurred during calcination in the heat treatment step due to sintering. By comparing the BET surface area, pore

Table 2
Crystallite size, reducibility, metal dispersion and coking content of as-synthesised 3 wt.% NiCo catalysts anchored on dual support (CeZrO$_2$–SiC) prepared *via* different methods.

Sample	Crystalline particle size (nm)	Reducibility (%)	Metal dispersion (%)	Amount of carbon in the fresh SiC support/Coking content in spent catalyst (%)[a]
Supports				
γ-Al$_2$O$_3$	10.4	–	–	–
CeZrO$_2$	5.7	59	–	–
SiC(lab)	7.4	–	–	30
SiC(SICAT)	20	–	–	30
3 wt.% NiCo catalysts anchored on single and dual supports				
CeZrO$_2$	6.3	35	9.1	1.1
2-Step γ-Al$_2$O$_3$–CeZrO$_2$	11.5	34	18.7	0.4
DI γ-Al$_2$O$_3$–CeZrO$_2$	15.2	20	–	3.0
WI γ-Al$_2$O$_3$–CeZrO$_2$	14.0	29	–	1.1
2-Step SiC(lab)–CeZrO$_2$	7.6	34	17.5	1.8
DI SiC(lab)–CeZrO$_2$	20	25	–	10
WI SiC(lab)–CeZrO$_2$	6.9	37	–	0.4
2-Step SiC(SICAT)–CeZrO$_2$	15	39	15.5	3.1
DI SiC(SICAT)–CeZrO$_2$	17	40	–	14
WI SiC(SICAT)–CeZrO$_2$	11	42	18.0	1.4

[a] Measured by CHNS and TPO. The final value was averaged from both analyses.

volume, pore width and skeletal density data of single *versus* dual supports, the values for the latter lie in between the values of the individual constituents.

The decrease of pore volume from 0.83 to 0.67 cm^3/g for γ-Al$_2$O$_3$ to γ-Al$_2$O$_3$–CeZrO$_2$, and from 0.44 to 0.34 cm^3/g for SiC(lab) to SiC(lab)–CeZrO$_2$ implies that the smaller particles have indeed entered the pores and formed deposits on the inner walls, causing a decrease in pore size [42]. This can be elucidated by transport phenomena for the 2-step sample that is ascribed to the DP process through the hydrolysis of urea. On the other hand, DI and WI rely on the adsorption–diffusion process based on coordination chemistry.

For fresh catalysts prepared after the deposition of NiCo metals on the support, in the set of γ-Al$_2$O$_3$-based catalysts, 2-step solids exhibit the highest BET surface area, followed by WI and then DI samples. In the set of SiC(lab)-based catalysts, WI has the highest BET surface area, followed by 2-step and then DI. In the set of SiC(SICAT)-based catalysts, 2-step has the highest BET surface area, followed by WI and then DI. This ranking can also be made by comparing values in Table 1. Their surface area is predominantly influenced by their support, as the SiC(lab) ones recorded the highest values (130–173 m^2/g), followed by γ-Al$_2$O$_3$ ones (83–117 m^2/g), and lastly SiC(SICAT) ones (38–58 m^2/g). The same

holds true for measured pore volume and skeletal density values. The range for skeletal density values in all samples does not vary greatly, *i.e.* 2.9–4.7 g/cm^3.

3.3. UV–Vis diffuse reflectance spectroscopy

Fig. 3 shows the UV–Vis diffuse reflectance spectra of fresh catalysts examined in the present study, with bands attributed to various species included at the top of Fig. 3 as well. As previously mentioned in the XRD analysis, the existence of NiAl$_2$O$_4$ and CoAl$_2$O$_4$ spinels was further investigated using this technique. In Fig. 3a, the presence of CoAl$_2$O$_4$ was detected by bands located at 551, 585 and 625 nm, which is its typical signature. These bands are attributed to different electronic transitions of Co^{2+} in tetrahedral environment (*i.e.* transition from the ground ^{4}A$_2$(F) to the excited ^{4}T$_1$(P) energy level) [43]. The presence of Co$_3$O$_4$, which is characterised by bands at 370–400 nm and 660–675 nm can be observed. However, the band at 660–675 nm is in the same region with CoAl$_2$O$_4$ and thus cannot be differentiated. Nevertheless, the band region at 370–400 nm is ascribed to Co$_3$O$_4$ [44]. This suggests the presence of coexisting Co$_3$O$_4$ and CoAl$_2$O$_4$ in the prepared samples [45]. Fig. 3a also presents NiAl$_2$O$_4$ with *d–d*
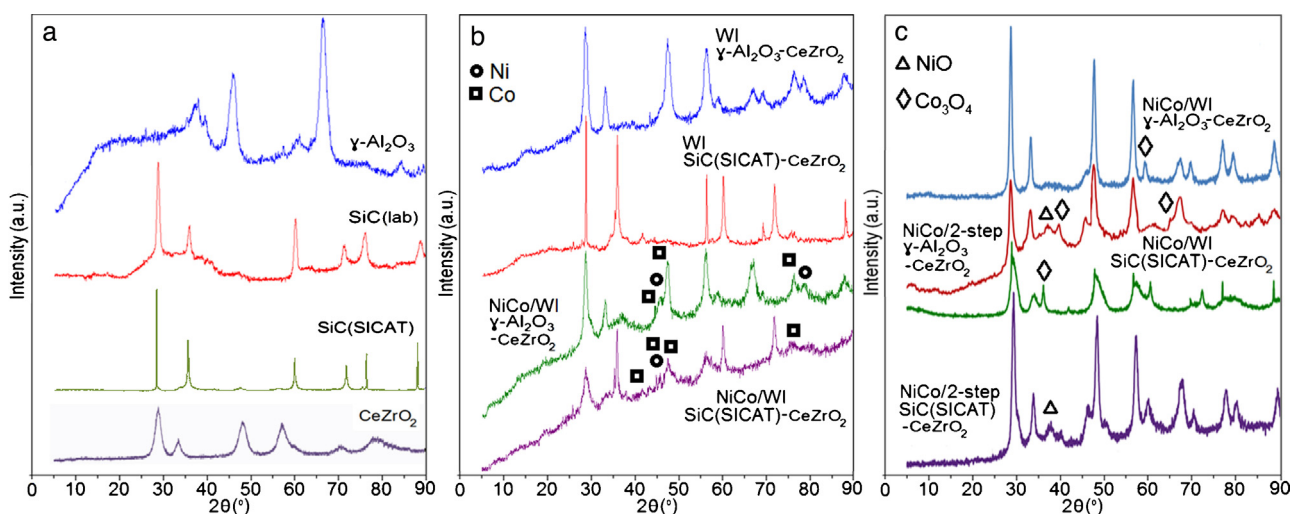

Fig. 2. XRD data for (a) the supports only (calcined single supports, prior to reduction), (b) fresh catalysts (obtained after 1 h reduction in H$_2$ atmosphere at 750 °C) and (c) spent catalysts after the 20 h CH$_4$–CO$_2$ DR activity tests.
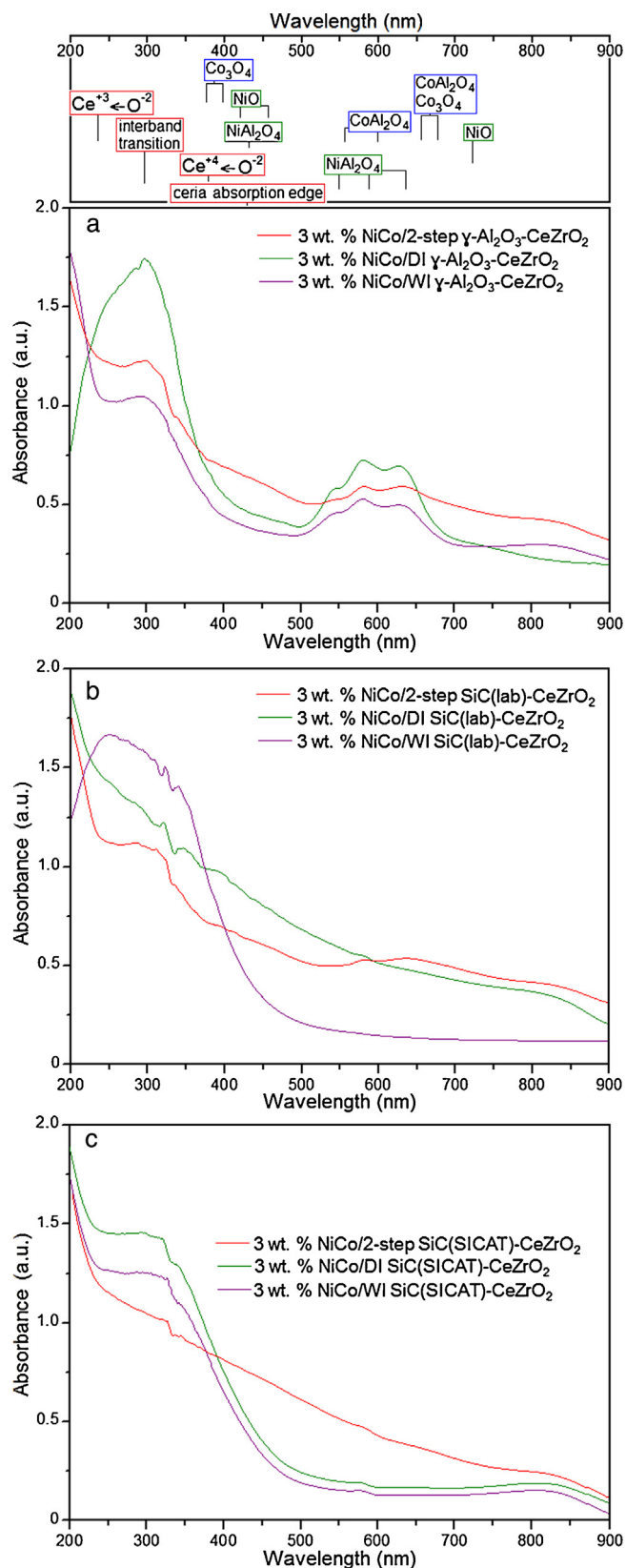
Fig. 3. UV–Vis diffuse reflectance spectra of the 3 wt.% NiCo catalysts supported on (a) γ-Al$_2$O$_3$–CeZrO$_2$, (b) SiC(lab)–CeZrO$_2$, and (c) SiC(SICAT)–CeZrO$_2$. The dual supports were synthesised by 2-step, DI and WI methods.

transition bands at 550 nm, characteristic of Ni^{2+} with tetrahedral symmetry. The phases of tetrahedral Ni^{2+} and the formation of NiAl$_2$O$_4$ are detected at 590 nm. Previous studies have shown that the colour of CoAl$_2$O$_4$ is strongly affected by the synthesis temperature [46,47]. Various catalyst pretreatment temperatures result in diverse extents of Ni and Co incorporation into the structure of alumina, which in turn, render varied predominant phases that ultimately determine the colour of the sample. The WI and 2-step NiCo/CeZrO$_2$–γ-Al$_2$O$_3$ catalysts are green, whilst the DI one is blue. It is suggested that the colour originates from the octahedral coordinated Co^{2+} in CoAl$_2$O$_4$ spinel [48,49]. Comparing the UV–Vis absorbance spectra for different samples (Fig. 3a), it can be noticed that in the spectrum of 3 wt.% NiCo/DI γ-Al$_2$O$_3$–CeZrO$_2$, the band at 300 nm dominates, in comparison to its counterparts. In this region, the signal due to O^{2-} → Ce^{4+} charge transfer is inferred, which implies the presence of ceria in the predominantly +4 oxidation state. Additionally, H$_2$-TPR results presented in Table 2 show the reducibility of this catalyst as the lowest amongst all, indicating the high stability of Ce in its +4 oxidation state in this particular sample.

Fig. 3b contains a broad band between 550 and 650 nm, with a peak centred at around 570 nm and a hump at 630 nm. These are assigned to d–d transitions of Ni^{2+} cations in octahedral symmetry such as in NiO nanoparticles [50,51]. The sharp edges at 384 nm observed in all figures evidence the presence of bulk NiO [52], since this is its characteristic band. In the 500–800 nm region for γ-Al$_2$O$_3$ and SiC(lab) supported catalysts, the bands corresponding to Ni^{2+} with tetrahedral symmetry were also detected [29]. The bands at 250 (for Fig. 3a–c) and 300 nm (for γ-Al$_2$O$_3$ and SiC(lab)) are assigned to charge transfer transitions that occurred for Ce^{3+} ← O^{2-} and Ce^{4+} ← O^{2-}, respectively [53]. Also, the spectra of samples in all figures show a broad band at 320–340 nm that is ascribed to the interband transitions of ceria [54].

Taking into account the large number of species that can be present, ions having different electronic and coordination environment, there are regions where bands due to Co$_3$O$_4$ and CoAl$_2$O$_4$ overlapped with bands due to NiO and NiAl$_2$O$_4$. However, distinction can be made as several wavelength regions are non-overlapping, in other words, exclusive. Considering Co$_3$O$_4$ as an example, its absorbance signals appear at 368 and 688 nm [55]. Meanwhile, CoAl$_2$O$_4$ is detected at 551, 585 and 625 nm (tetrahedral coordination). NiAl$_2$O$_4$ is detected at 430, 550, 590 and 640 nm (tetrahedral symmetry), and 380 nm (octahedral symmetry), whereas NiO is detected at 420, 465 and 720 nm. In conclusion, different preparation procedures (DI, WI, 2-step DP) gave rise to spectra with different intensities, but mostly with similar characteristics.

3.4. Raman spectroscopic analysis

Fig. 4 depicts the Raman spectra of 3 wt.% NiCo on 2-step γ-Al$_2$O$_3$–CeZrO$_2$ and WI SiC(SICAT)–CeZrO$_2$. For 2-step γ-Al$_2$O$_3$-based catalyst (Fig. 4a), the intense γ-Al$_2$O$_3$ band at 4079 cm^{-1} from the fresh catalyst subsided substantially in the spent sample. Although Raman scattering is sourced from both the surface and bulk of a solid, the signal from the bulk is attenuated when the sample strongly absorbs the excitation laser light and the scattering light. Thus, the Raman spectra contain more signals from the surface region than the bulk. In particular, most transition metal oxides (such as NiCo in our case), strongly absorb UV laser light, so UV Raman spectroscopy is more sensitive to the surface region. Peaks at 1238 and 1341 cm^{-1} correspond to C-C stretching modes. In addition to that, it is observed that the appearance of graphitic carbon at 1578 cm^{-1} for the spent sample did not surface previously in the fresh sample. The Raman spectra at energies
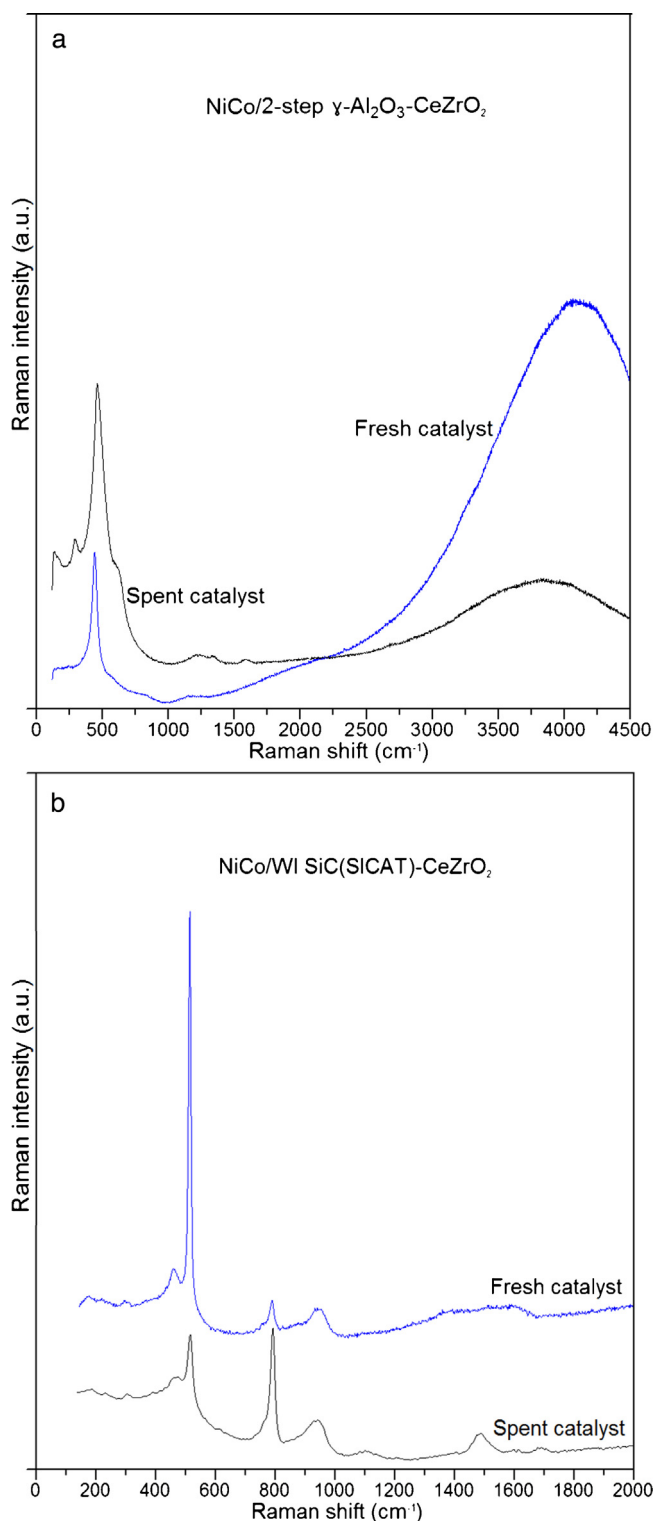
Fig. 4. Raman spectra of (a) 3 wt.% NiCo/2-step γ-Al$_2$O$_3$/CeZrO$_2$, and (b) 3 wt.% NiCo/SiC(SICAT)/CeZrO$_2$ for fresh and spent samples (after 20-h DR activity test).

around that of the F$_{2g}$ peak measured between 200 and 650 cm^{-1} also confirm the presence of lattice defects after Zr was introduced into the ceria–zirconia mixed oxide network, as evidenced by XRD of the fresh calcined samples and the single support (Figs. Fig. 1 and 2a, respectively). It is clear that upon exposure to high reaction temperature, the F$_{2g}$ peak has shifted from 442 cm^{-1} in the fresh to 464 cm^{-1} in the spent catalyst. This, however, does not imply the

destruction of the ceria–zirconia solid solution as it is very stable under dry reforming conditions. This is because the corresponding XRD diffractograms for this crystalline compound can still be visibly seen in the spectra of the spent samples (Fig. 2c) [56,57].

For WI SiC(SICAT)-based catalyst (Fig. 4b), the 303 cm^{-1} band on both the fresh and spent samples is possibly derived from oxidised Si from the SiC [58]. This peak is slightly more intense in the spent sample. The band at 460 cm^{-1} belongs to ceria and represents one of the triply degenerate Raman F$_{2g}$ modes. It is a symmetric, breathing vibrational mode of the O anions around each Ce cation [59]. It is worth noting that this mode is very sensitive to the oxygen sub-lattice disorder resulting from exposure to the continuous reducing/oxidising (H$_2$-rich/H$_2$O-rich) atmospheres that were present in the DR reaction. This balanced dynamics of oxygen capture and release from ceria could very well be the reason for the sustained activity of the catalyst over a longer period of time, as demonstrated in its 550 h stability test (Fig. 9). The band at 460 cm^{-1} was sharper in the fresh but broadened in the spent sample. Broadening of the F$_{2g}$ band at 467 cm^{-1} indicates increased structural disorder of the oxygen sub-lattice in the Ce$_{0.75}$Zr$_{0.25}$O$_2$ solid solution. Raman analysis clearly points out a decrease of M-O bond symmetry in the analysed samples during prolonged exposure to the DR reaction conditions. The most outstanding peak in Fig. 4b is the extremely sharp, narrow and strong peak at 499 cm^{-1}. It is characteristic of Si–Si transverse optic mode (TO) from SiC and it weakened tremendously in the spent catalyst [60]. Conversely, the peak at 789 cm^{-1} that is attributed to water vibrational mode has increased in the spent catalyst as compared to the fresh sample [61] due to the presence of water vapour (about 10 mol. % formed *via* the reverse water gas shift (RWGS) reaction that was at play during the activity test (Fig. 7c). The presence of carbon nanotubes can be ascertained due to peaks in the 1500–1605 cm^{-1} range, representing G-band optical mode E_{2g} of graphite–an intrinsic feature that is closely related to vibrations in all sp^2 carbon materials [62]. This is also verified by SEM microscopy (Fig. 8f).

In conclusion, different supports (γ-Al$_2$O$_3$ and β-SiC) can be distinguished by the different Raman bands. The bands for CeZrO$_2$ solid solution in both catalysts were detected, but the intensities varied. Same applies for fresh *versus* spent samples. As for the metal active phase, there are differences as well. For instance, the emerged shoulder in the spent sample of γ-Al$_2$O$_3$-based catalyst (that was not present in the fresh) at ∼570 cm^{-1} indicates the appearance of NiO. This is also in line with the XRD spectra for the spent samples in Fig. 2c.

3.5. Physicochemical properties of supported catalysts

The reducibility, metal dispersion and carbon content of supports (single) were tabulated in Table 2. For the measured reducibility, CeZrO$_2$ single support *per se* exhibits the highest value of 59%. The reducibility percentage for the support was calculated from $[(m_0 - m_1)/m_0]/0.0497 \times 100\%$, where m_0 and m_1 represent sample mass before and after reduction in H$_2$, and where 0.0497 is the theoretically achievable weight change for a CeZrO$_2$ material with a ce:Zr = 80:20 chemical composition (in which all Ce^{4+} is transformed into Ce^{3+}). As for the calculation of the catalyst reducibility, firstly, the reduction of NiO and Co$_3$O$_4$ was assumed to be completed during the reduction process. The amount of H$_2$ required for the reduction of Ni and Co active metals was calculated based on the actual Ni and Co content in the samples. The remaining amount of consumed H$_2$ was attributed to the reduction of CeO$_2$ and this was compared to the value that is required for the complete Ce^{4+} transformation into Ce^{3+}, based on the actual content of CeO$_2$ in the investigated sample. Redox properties of CeZrO$_2$ decreased after the addition of γ-Al$_2$O$_3$, β-SiC and NiCo. Their reducibility values span across 20–42%. This can be attributed to

the reduced surface area, in addition to the crystallite size increase caused by sintering of the $CeZrO_2$ phase during subsequent calcination steps, after the deposition of either the second support component (γ-Al_2O_3 or β-SiC) and NiCo active metal phases. Also, it is worthwhile to note that the temperature and metal loading values used in this work favour NiCo alloy formation based on established phase diagrams [63]. As Ce^{4+} was reduced to Ce^{3+}, the reduced surfaces (in which oxygen vacancies were present) were obtained for the support. The charge transfer from ceria to the metal particles induced electronic effect that led to a chemical modification of the metal atoms and thus good metal–support interaction, favourable for catalytic reactions [64]. The reducibility of $CeZrO_2$ solid solutions is known to depend on the mentioned morphological properties [18]. Moderate metal dispersion of Ni and Co (16–19%) was obtained by CO pulse chemisorption. This is because when NiCo metals were loaded on $CeZrO_2$, metal particles interacted with the Ce^{4+}/Ce^{3+} cation pairs. The charge transfer in ceria was also ascertained by UV–Vis spectroscopy as shown in Fig. 3. Carbon content in the spent catalysts recorded for all materials after the 20-h DR tests was between 0.4 and 3.1 wt.%, demonstrating very encouraging results as shown in Table 2. The following ranking in terms of increasing selectivity for coke accumulation can thus be established: 2-step γ-Al_2O_3–$CeZrO_2$, WI SiC(lab)–$CeZrO_2$ < WI γ-Al_2O_3–$CeZrO_2$ < WI SiC(SICAT)–$CeZrO_2$ < 2-step SiC(lab)–$CeZrO_2$.

To summarise, the preparation method of each mixed support has a considerable impact on the properties of the final fresh calcined catalyst, because the reducibility and metal dispersion values varied. However, it is suggested that the ordered phases within each specimen are similar to each other, since the XRD diffraction pattern for each set of support is identical (Figs. 1 and 2). For 2-step γ-Al_2O_3–$CeZrO_2$, SiC(lab)–$CeZrO_2$, SiC(SICAT)–$CeZrO_2$ and WI SiC(lab)–$CeZrO_2$ solids, the considerably small particle size (7.6–15 nm) likely resulted from good NiCo dispersion (16–19%) over the support surface. Having smaller NiCo clusters likely induced stronger metal–support interactions, especially with reducible ceria. Thus, high OSC originating from ceria gave rise to high reducibility for the catalysts (34–42%), enabling low coking in the 20-h activity tests (0.4–3.1 wt.%).

3.6. 20-h DR activity tests

Fig. 5 shows the reaction effluent concentration (%) *vs.* 20-h time on stream (TOS) for catalytic testing of 3 wt.% NiCo on $CeZrO_2$/γ-Al_2O_3, with the dual support prepared by various methods. Promising performances of solids are shown in Fig. 5a–c. In comparison with other catalytic compositions and our previous results, candidates of Fig. 5a–c have higher stability [4,20,22,57]. In terms of H_2/CO ratio, RWGS accounts for the wider gap that emerged between H_2 and CO in the 2-step and DI γ-Al_2O_3-based catalysts than the WI γ-Al_2O_3-based ones. The WI-based catalyst exhibits high H_2/CO ratio. H_2 and CO yields recorded for the most promising NiCo/2-step γ-Al_2O_3–$CeZrO_2$ catalyst were 71% and 81%, respectively. Although the calcined spinels were inactive in the fresh catalysts as shown from previous work reported by Al-Ubaid et al. [65], their reduced forms have led to significant activity and stability, which is in line with our results. This is because the spinel layers on these catalyst as seen in XRD (Fig. 1a) did not exist after 1-h reduction in H_2 at 750 °C before the DR activity test (Fig. 2b) [36,37]. It is likely that the Ni and Co atoms that were incorporated into the Al_2O_3 structures which formed the $NiAl_2O_4$ and $CoAl_2O_4$ spinels cannot catalyse the DR reaction (as it cannot be accessed by the CH_4 and CO_2 gas molecules). However, once the samples were reduced, the metals were liberated from the alumina, thereby resulting in the decoration of the Al_2O_3 surface with individual Ni and Co atoms, which can aggregate and form Ni and Co clusters (16–19% NiCo dispersion, as measured by CO on the reduced

samples in Table 2). These clusters are metallic, present on the outer surface of the Al_2O_3 and/or $CeZrO_2$ support and therefore are functional. Consequently, the spinel structure disappeared and the catalyst was activated after the reduction. Moreover, metal oxide-support interactions (strong due to reducible ceria) contributed to high activity, stability and resistance to coking [19,66].

Fig. 6 shows the reaction effluent concentration (%) *vs.* 20-h time on stream (TOS) for catalytic testing of 3 wt.% NiCo on $CeZrO_2$/SiC(lab) dual supported catalysts. 2-Step SiC(lab)-based catalyst produced a steady concentration of H_2 at 25–27% and CO at 32–35%. All catalysts exhibited an initial drop of activity due to possible sintering of $CeZrO_2$/SiC or NiCo particle agglomeration. It can be noticed that deactivation occurred for DI SiC(lab) catalyst as shown by the apparent and continuous decline in H_2 selectivity (Fig. 6b). It continued from the beginning until the end of the test. This suggests that during catalyst preparation, the metal precursors of Ce and Zr did not permeate well through the pores of the SiC. As a result, the lowest activity was observed for this material. In Fig. 6c, WI SiC(lab)–$CeZrO_2$ sample depicts the best catalytic performance in terms of activity as well as exceptional stability, followed by the 2-step sample. This could be elucidated by the efficient containment of $CeZrO_2$ and NiCo clusters within the pores of the WI SiC(lab) support, and this therefore imparted better NiCo dispersion.

Fig. 7 displays the reaction effluent concentration (%) *vs.* 20-h time on stream (TOS) for catalytic testing of 3 wt.% NiCo on $CeZrO_2$/SiC(SICAT). 2-Step $CeZrO_2$/SiC(SICAT) catalyst shows good stability and high concentration of syngas (H_2 = 32–33 vol.%; CO = 41–42 vol.%) (Fig. 7a). By calculations, the syngas yield in 2-step $CeZrO_2$/SiC(SICAT) catalyst is: H_2 = 77%, CO = 90%. DI synthesis method is hypothesised to result in only partial permeation of Ce and Zr precursors into the pore network of SiC, which led to a noticeable catalyst deactivation and low CH_4 and CO_2 conversions, as seen in Fig. 7b. Furthermore, Fig. 7c which shows the behaviour of WI sample has the most stable profile of all catalysts. Its high activity is comparable to the 2-step sample, in which all gas composition amounts are similar, but with better stability. It is remarkable that even with low BET surface area of 38 m^2/g and low pore volume of 0.08 cm^3/g (lowest of all fresh catalysts prepared in our work), high conversions of CH_4 and CO_2 (91 and 92%, respectively) were accomplished. The hydrophobic nature of SiC intrinsically deterred water adsorption on the supported catalysts [67]. It could also retard undesirable side reactions such as the RWGS process and facilitate the preservation of Ni and Co clusters in an unoxidised, active metallic form. Since the SiC(SICAT) support is extremely resistant towards high temperature, sintering was less pronounced (as shown in its lowest decrease of surface area when compared to other spent catalysts in Table 3). Its mechanical strength maintained the entire catalyst structure in its original form for effective functioning throughout the DR reaction process. This additional functionality was not provided in our previous catalysts with only $CeZrO_2$ as the single support [20,22]. Clearly, this shows that the dual support approach is superior in maintaining high and stable catalytic activity in the DR reaction. Based on the 20-h activity tests, 2-step and WI provide better materials than DI. Thus, catalysts prepared using these methods were chosen for prolonged DR examination.

3.7. Characterisation of surface morphology for fresh and spent catalysts

Fig. 8 shows the surface morphology of fresh and spent (a,b) NiCo/WI $CeZrO_2$-γ-Al_2O_3, (c,d) NiCo/WI $CeZrO_2$-SiC(lab) and (e,f) NiCo/WI $CeZrO_2$-SiC(SICAT) catalysts as characterised *via* SEM imaging. Since there was no structurally significant differences amongst catalysts prepared by DI, WI or 2-step procedures,
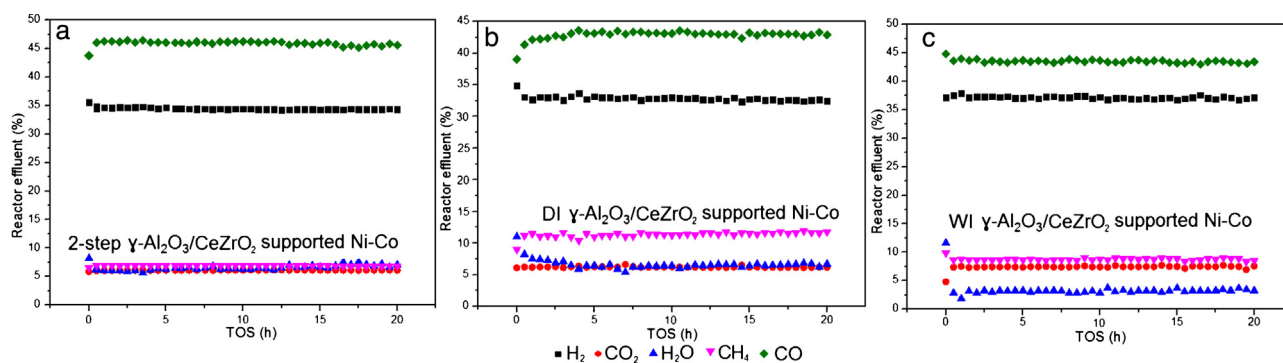
Fig. 5. Reactor effluent (vol.%) *vs.* 20-h time on stream (TOS) for 3 wt.% NiCo catalysts supported on γ-Al$_2$O$_3$/CeZrO$_2$, with the dual support prepared by means of (a) 2-step deposition precipitation, (b) dry impregnation and (c) wet impregnation method.
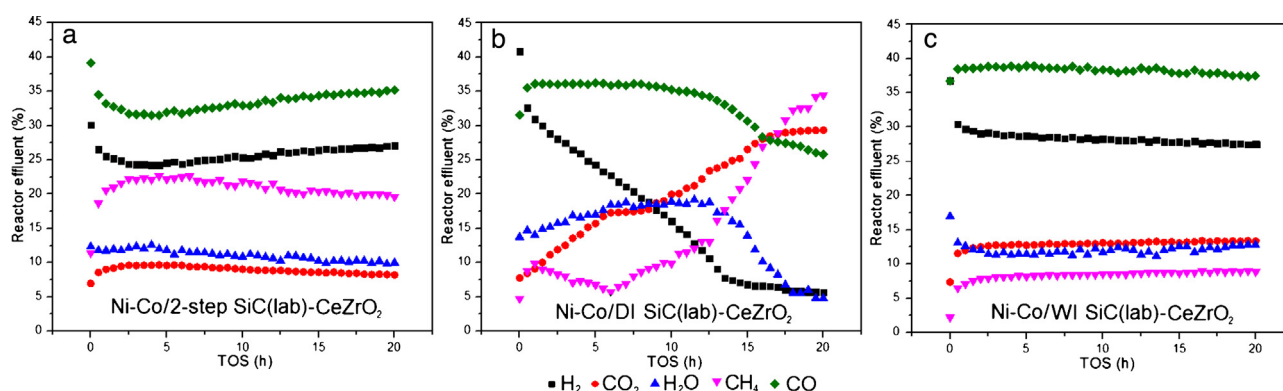

Fig. 6. Reactor effluent concentration (vol.%) *vs.* 20-h time on stream (TOS) for 3 wt.% NiCo catalysts supported on SiC(lab)/CeZrO$_2$, using electrophoretically synthesised SiC, with the dual support prepared by means of (a) 2-step deposition precipitation, (b) dry impregnation and (c) wet impregnation.
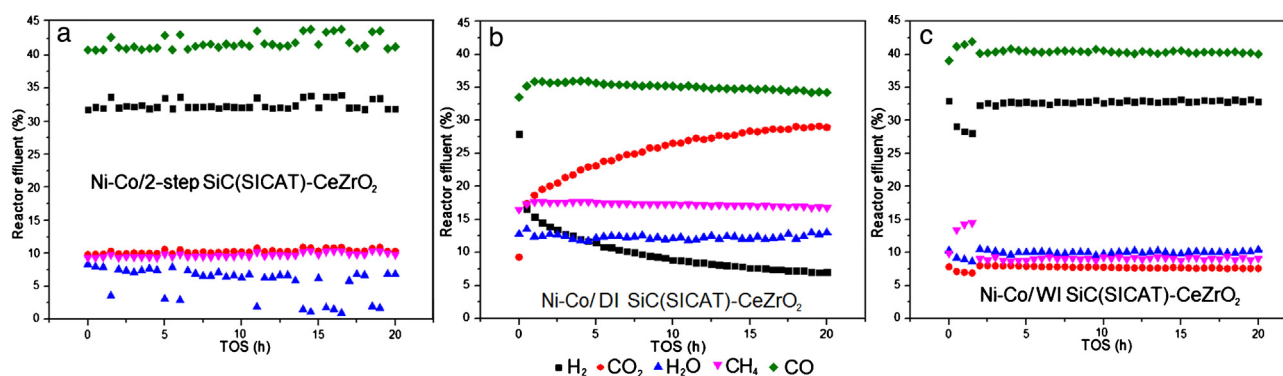

Fig. 7. Reactor effluent (vol.%) *vs.* 20-h time on stream (TOS) for 3 wt.% NiCo catalysts supported on SiC/CeZrO$_2$, using SiC obtained from SICAT, and the dual support prepared by means of (a) 2-step deposition precipitation, (b) dry impregnation and (c) wet impregnation method.

Table 3
Textural properties of spent catalysts after 20-h DR reaction—3 wt.% NiCo catalysts anchored on dual supports (CeZrO$_2$–SiC) prepared *via* different methods.

Spent catalyst	S_{BET} (m^2/g)	V_{pore} (cm^3/g)	d_{pore} (nm)	$\rho_{skeletal}$ (g/cm^3)
2-Step CeZrO$_2$/γ-Al$_2$O$_3$	63.7	0.35	19.8	4.53
DI CeZrO$_2$/γ-Al$_2$O$_3$	93.2	0.59	22.4	3.58
WI CeZrO$_2$/γ-Al$_2$O$_3$	60.5	0.38	23.1	3.86
2-Step CeZrO$_2$/SiC(lab)	49.2	0.13	10.4	4.14
DI CeZrO$_2$/SiC(lab)	23.4	0.08	12.8	2.90
WI CeZrO$_2$/SiC(lab)	31.3	0.06	7.6	2.88
2-Step CeZrO$_2$/SiC(SICAT)	22.1	0.09	12.3	3.02
DI CeZrO$_2$/SiC(SICAT)	26.6	0.07	9.8	2.82
WI CeZrO$_2$/SiC(SICAT)	14.0	0.04	11.8	3.36
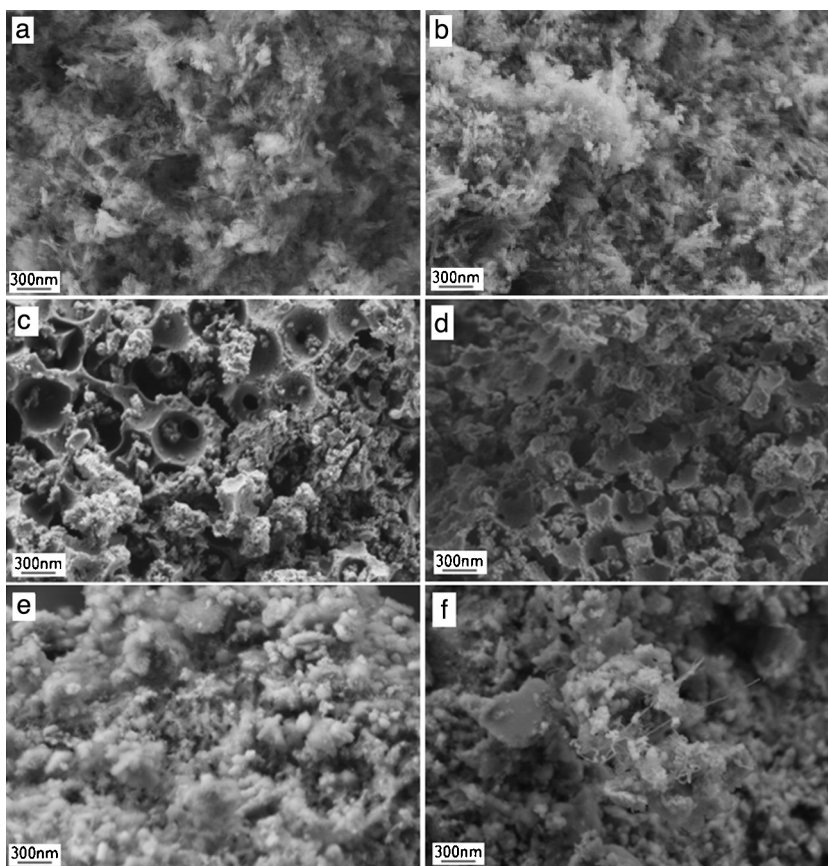
Fig. 8. SEM micrographs of (a) fresh and (b) spent 3 wt.% NiCo/WI CeZrO$_2$–γ-Al$_2$O$_3$ catalyst, (c) fresh and (d) spent 3 wt.% NiCo/WI CeZrO$_2$-SiC(lab) catalyst, as well as of (e) fresh and (f) spent 3 wt.% NiCo/WI CeZrO$_2$–SiC(SICAT) catalyst.

typical representative samples were displayed from WI CeZrO$_2$/γ-Al$_2$O$_3$, WI CeZrO$_2$/SiC(lab) and WI CeZrO$_2$/SiC(SICAT) (*i.e.* prepared by means of wet impregnation). Fig. 8a exhibits abundant amount of tiny, 2D flaky, flat sheets of alumina, intermixed with nanocrystalline porous CeZrO$_2$. The dispersion of NiCo phase over CeZrO$_2$/γ-Al$_2$O$_3$ was about 18%, as presented in Table 2. This suggests the average diameter of dispersed bimetallic particles to be about 5 nm, which is outside the range for conclusive imaging with SEM–EDX analysis. This is also consistent with XRD results (Fig. 1), since no peaks belonging to metallic Ni and Co clusters were detected in the fresh calcined samples, indicative of the invariably low decrease in metal dispersion. The obtained results also infer that the migration of active metal particles was low, and that the metal growth is not significant in the DR process. In Fig. 8b, tiny, bead-like, spherical forms of carbon (<30 nm) were observed, in which its composition was verified by EDXS. Their presence was also previously confirmed by Raman analysis for the spent catalysts (Fig. 4a). In Fig. 8c, ordered macroporous structure of SiC with a pore diameter measuring at approximately 400 nm, partially covered with irregular porous CeZrO$_2$ nanoparticle agglomerates, is visible. Fig. 8d displays the largely calcined SiC structures due to high reforming temperature. However, original structures for CeZrO$_2$ and macroporous SiC were retained. Although the thickness of the pore walls is in the order of several nanometres, good mechanical stability is demonstrated as indirectly seen from the compact macroscopic structure shown in Fig. 8d. Much larger aggregates were seen in and around the broken cavities of the SiC. This implies that CeZrO$_2$ nanoparticles were successfully immobilised. Another evidence for this is supported by XRD diffractograms of the spent catalysts, in which CeZrO$_2$ peaks remain clearly seen (Fig. 2c). In Fig. 8e, the porous sample shows SiC(SICAT)-based catalyst before

and after the DR reaction. Again, the existence of NiCo metal particles due to their very low amount and phase contrast is ambiguous. Nevertheless, they were detected from EDXS measurements (Table S1, Supplementary data). Thus, it is inferred that these catalysts contain good metal dispersion, in which the measured value was also shown previously in Table 2. In Fig. 8f, filamentous carbon was detected, measuring approximately 1.2 μm in length and on average 10 nm in width. The carbon presence in the spent catalyst was verified previously using Raman analysis (Fig. 4b).

3.8. Textural properties of spent catalysts

Textural properties of the spent catalysts after 20-h DR reaction for 3 wt.% NiCo catalysts on dual supports (CeZrO$_2$–SiC) prepared *via* different methods were listed in Table 3. All catalysts underwent reduction in BET surface area, pore volume (except for DI γ-Al$_2$O$_3$–CeZrO$_2$), increase in pore size (except for DI SiC(SICAT–CeZrO$_2$)) and decrease in skeletal density, as observed in Table 1 for comparison. The reduction in BET surface area spans a very broad range, *i.e.* from 11 to 82%. In particular, extensive sintering is observed for SiC(lab)-based catalysts as their surface area underwent a substantial decrease, namely, 54–82%. γ-Al$_2$O$_3$-based catalysts were affected the least. Likewise for pore volume data in Table 1, the pore volume of spent catalysts, although decreased a little, is the highest for γ-Al$_2$O$_3$ based solids (Table 3). Interestingly, DI CeZrO$_2$/γ-Al$_2$O$_3$ solid underwent a 35% increment in its pore volume. Although DI profile is as good as the 2-step one, its carbon content is 7.5 times of the latter. This allows for the explanation that the formed carbon nanotubes resulted in the generation of additional porosity, which can be identified using N$_2$ sorption technique. As for changes in skeletal density, the deviation
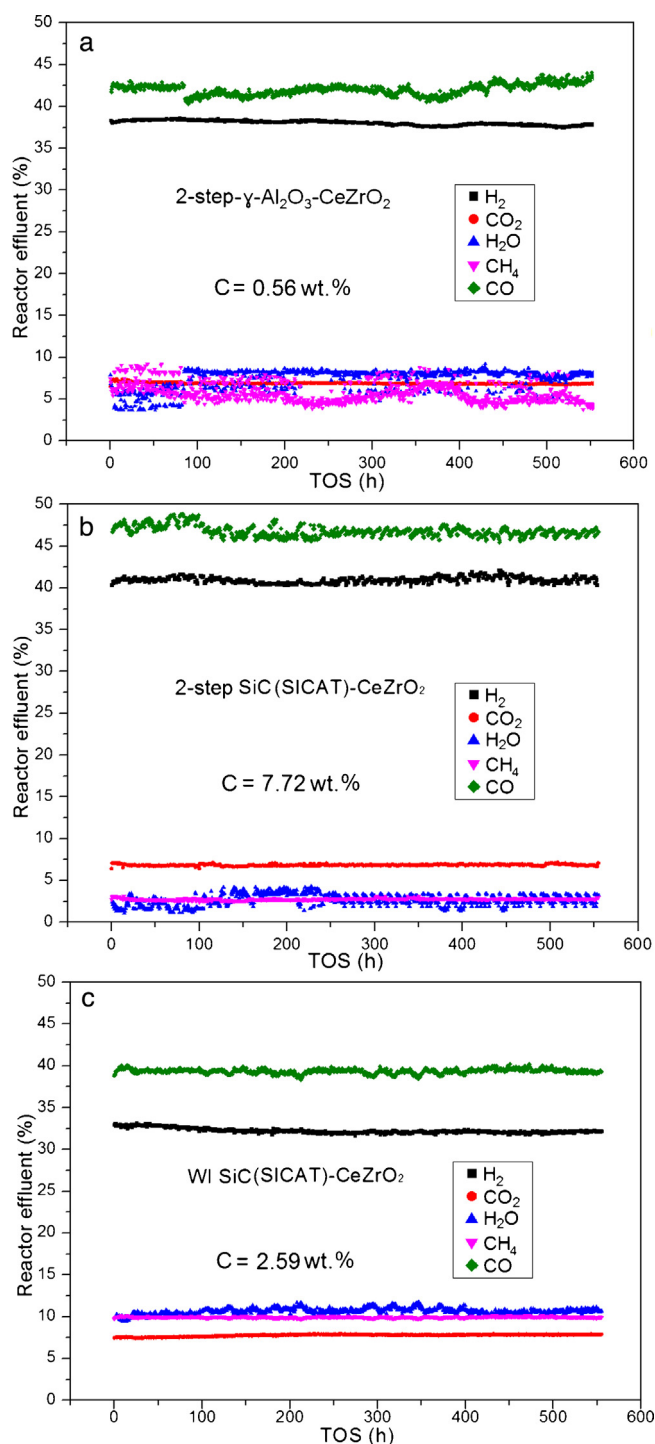
Fig. 9. 550-h stability tests for the three most promising 3 wt.% NiCo catalysts supported on (a) γ-Al₂O₃/CeZrO₂ prepared by 2-step DP, (b) SiC(SICAT)/CeZrO₂ (2-step DP) and (c) SiC(SICAT)/CeZrO₂ (WI), with the coke content for each displayed on the graph.

3.9. Long-term stability tests

In Fig. 9, results of 550-h stability tests are illustrated for the most promising catalysts, namely, 3 wt.% NiCo catalysts supported on (a) γ-Al₂O₃/CeZrO₂ (2-step DP), (b) SiC(SICAT)/CeZrO₂ (2-step DP), and (c) SiC(SICAT)/CeZrO₂ (WI). The activity profiles are shown, with the accumulated coke amount for each catalyst displayed on the graph. Exceptionally stable catalytic performance and high selectivity for syngas was observed, supporting the results of the 20 h activity tests. This is due to the synergistic effect of the bimetallic system and the effect of dual support to effectively preserve the dispersed CeZrO₂ and NiCo phases. Although the active NiCo particles were hardly detected by XRD in their calcined, unreduced state, they were actually present in highly dispersed form and in the aluminate structure (Fig. 1a). Since the catalyst was reduced at a high temperature of 750 °C, the formation of surface spinels, such as $NiAl_2O_4$ and $CoAl_2O_4$ could induce a positive effect on the suppression of carbon deposition [68], thereby contributed to the remarkably low coke content of 0.56 wt.% at the end of the 550-h test. Moreover, the water content during the test is about 7–10%. This is because γ-Al₂O₃ *per se* exhibits minor activity for CH_4 and CO_2 dissociation. Its surface highly populated with hydroxyl species and the concurrent presence of substantial amounts of gaseous H_2, CO and CO_2 can contribute considerably to the overall RWGS extent, and as such, influence the overall product distribution of DR reaction. On the other hand, contribution from SiC in the dual support, beside spatial separation and thermal immobilisation of active components, is negligible. Hence, water production was considerably lower when SiC support was used. The fact that SiC with its low surface area (Table 1) and moderate dispersion of NiCo clusters (Table 2) successfully survived the 550-h long term test reflects an unconventional phenomenon, defying the usual concept regarding criteria for support that best creates a conducive environment for high activity supposedly are: activated metallic particles with small particle size, and those with maximised surface area for high metal dispersion. Moreover, in order to further confirm the long-term stability of the catalyst, harsh conditions in which oxygen source was scarce in the DR reaction were employed as well. By feeding reactant gases at a ratio higher than 1, *i.e.* $CH_4/CO_2 = 60/40$, a stable and active profile was achieved for the 3 wt.% NiCo/WI SiC–CeZrO₂ catalyst. Furthermore, carbon content of only 0.47 wt.% was obtained for the spent catalyst from TPO analysis (Fig. S3, Supplementary data).

In summary, with the aid of γ-Al₂O₃ and SiC introduced into the CeZrO₂ support, the severity of ceria losing its OSC due to surface area loss under high temperature calcination and reduction can be mitigated. Not only can CeZrO₂ be perceived as a support for the active metal phase, it can participate as an active component in the complex catalytic system to a higher extent than γ-Al₂O₃ or especially SiC which is inert. As for the SiC of the dual support, it improves NiCo anchoring due to its high thermal resistance. These catalysts demonstrated more stable catalytic performances than our previous ones on CeZrO₂ single support [20,22,56], thereby amplifying the added value of γ-Al₂O₃ and SiC into the support.

4. Conclusions

This work reports on the progress of CH_4–CO_2 dry reforming (DR) using NiCo catalysts dispersed on CeZrO₂ combined with either γ-Al₂O₃ or β-SiC as a dual support synthesised *via* basic and facile methods, *i.e.* dry (DI), wet impregnation (WI) and 2-step deposition precipitation (DP). For γ-Al₂O₃, DI, WI and 2-step DP catalysts were highly active during 20-h DR reaction. The high reducibility and stability are due to the presence of Ni and Co aluminate species and CeZrO₂ solid solution (as confirmed by XRD and

from the initial values can be due to various reasons, including the transformation of oxide phases to metallic phases, catalyst sintering and the generation of closed pores, elimination of structural defects and stacking faults, polymorphism, rearrangement of amorphous to crystalline structure and the growth of carbon nanotubes. In terms of texture stability during the DR reaction, the best support is γ-Al₂O₃–CeZrO₂ prepared by 2-step deposition precipitation.

UV–Vis spectroscopy). The latter contributed to low carbon content in the spent catalysts, indicating very mild coking occurrence. DI which consists of pore volume filling shows mediocre results for SiC (hydrophobic support), albeit good performance for γ-Al$_2$O$_3$-based solids (hydrophilic support), as SiC only allows for a partly efficient metal deposition when water is used as a solvent. The 2-step γ-Al$_2$O$_3$–CeZrO$_2$, WI and 2-step SiC(SICAT)–CeZrO$_2$ catalysts are active and durable for up to 550 h. This remarkable achievement is ascribed to the excellent chemical/mechanical resistance of γ-Al$_2$O$_3$ and β-SiC, strengthened NiCo anchoring on these dual supports due to reducible ceria, which in turn, inhibited NiCo migration on their surface, thereby giving rise to good metal–support interaction. Hence, 2-step DP and WI are elegant synthetic routes for preparing the dual supports. As compared to our previous NiCo/CeZrO$_2$ catalysts, this work successfully demonstrated a step forward in the development of more robust catalysts with high activity and maximal carbon tolerance over a long duration (>3 weeks) without any deactivation by the introduction of γ-Al$_2$O$_3$ and SiC in CeZrO$_2$ as a dual support.

Acknowledgements

Appendix A. Supplementary data

Supplementary data associated with this article can be found, in the online version, at http://dx.doi.org/10.1016/j.apcatb.2014.09.012.

References

[1] S.L. Sun, N. Tsubaki, K. Fujimoto, Appl. Catal., A: Gen. 202 (2000) 121–131.
[2] N. Tsubaki, M. Ito, K. Fujimoto, J. Catal. 197 (2001) 224–227.
[3] K. Takanabe, K. Nagaoka, K. Nariai, K.-i. Aika, J. Catal. 232 (2005) 268–275.
[4] M.-S. Fan, A.Z. Abdullah, S. Bhatia, ChemCatChem 1 (2009) 192–208.
[5] M. Pilar Yeste, J.C. Hernández-Garrido, D. Carolina Arias, G. Blanco, J.M. Rodríguez-Izquierdo, J.M. Pintado, S. Bernal, J.A. Pérez-Omila, J.J. Calvino, J. Mater. Chem., A 1 (2013) 4836–4844.
[6] H. Ranjan Sahu, G. Ranga Rao, Bull. Mater. Sci. 23 (2000) 349–354.
[7] J. Ashok, S. Kawi, ACS Catal. 4 (2014) 289–301.
[8] F. Rodriguez-Reinoso, A. Sepulveda-Escribano, in: P. Serp, J. Luis Figueiredo (Eds.), Carbon Materials for Catalysis, John-Wiley and Sons, Inc., 2009, pp. 131–150.
[9] H. Wang, S. Zaidi, in: S.L. Suib (Ed.), New and Future Developments in Catalysis: Activation of Carbon Dioxide, Elsevier Ltd, 2013, pp. 445–480.
[10] J. Zhang, H. Wang, C. Xi, M. Shakouri, Y. Hua, A.K. Dalai, in: A.K. Dalai (Ed.), Nanocatalysis for Fuels and Chemicals, American Chemical Society, 2012, pp. 195–221.
[11] M.C.J. Bradford, M.A. Vannice, Catal. Rev.: Sci. Eng. 41 (1999) 1–42.
[12] F. Liao, S.L. Girshick, W.M. Mook, W.W. Gerberich, M.R. Zachariah, Appl. Phys. Lett. 86 (2005) 171913–171915.
[13] R.Q. Yang, C. Xing, C.X. Lu, L. Shi, N. Tsubaki, Appl. Catal., A: Gen. 385 (2010) 92–100.
[14] E.A. Burgemeister, W. von Muench, E. Pettenpaul, J. Appl. Phys. 50 (1979) 5790–5794.
[15] Y.T. Yang, K.L. Ekinci, X.M.H. Huang, L.M. Schiavone, M.L. Roukes, C.A. Zorman, M. Mehregany, Appl. Phys. Lett. 78 (2001) 162–164.
[16] P. Nguyen, C. Pham, Appl. Catal., A: Gen. 391 (2011) 443–454.
[17] D.L. Nguyen, P. Leroi, M.J. Ledoux, C. Pham-Huu, Catal. Today 141 (2009) 393–396.
[18] P. Djinović, I.G. Osojnik Črnivec, B. Erjavec, A. Pintar, ChemCatChem 6 (2014) 1652–1663.
[19] P. Djinović, I.G. Osojnik Črnivec, B. Erjavec, A. Pintar, Appl. Catal., B: Environ. 125 (2012) 259–270.
[20] M.S. Aw, I.G. Osojnik Črnivec, A. Pintar, Catal. Sci. Technol. 4 (2014) 1340–1349.
[21] D.S. Maciver, H.H. Tobin, R.T. Barth, J. Catal. 2 (1963) 485–497.
[22] M.S. Aw, I.G. Osojnik Črnivec, A. Pintar, Catal. Commun. 52 (2014) 10–15.
[23] V. Piriyawong, V. Thongpool, P. Asanithi, P. Limsuwan, J. Nanomater. 2012 (2012) (Article ID 819403, 6 pages).
[24] H.St.C. O'Neill, W.A. Dollase, C.R. Ross II., Phys. Chem. Miner. 18 (1991) 302–319.
[25] Z. Xu, Y. Li, J. Zhang, L. Chang, R. Zhou, Z. Duan, Appl. Catal., A: Gen. 213 (2001) 65–71.
[26] P.H. Bolt, F.H.P.M. Habraken, J.W. Geus, J. Solid State Chem. 135 (1998) 59–69.
[27] JCPDS—Inter Center for Diffraction Data 44, 160.
[28] JCPDS—Inter Center for Diffraction Data 42, 1300–1467.
[29] A.M. Becerra, A.E. Castro-Luna, J. Chil. Chem. Soc. 50 (2005) 465–469.
[30] Y. Li, Q. Fu, M. Flytzani-Stephanopoulos, Appl. Catal., B: Environ. 27 (2000) 179–191.
[31] Y. Zhang, X. Han, K. Zheng, Z. Zhang, X. Zhang, J. Fu, Y. Ji, Y. Hao, X. Guo, Z. Wang, Adv. Funct. Mater. 17 (2007) 3434–3435.
[32] F.-L. Wang, L.-Y. Zhang, Y.-F. Zhang, Nanoscale Res. Lett. 4 (2008) 153–156.
[33] N. Sergent, J. Lamonier, A. Aboukais, Chem. Mater. 12 (2000) 3830–3835.
[34] J. Häglund, A. Fernández Guillermet, G. Grimvall, M. Körling, Phys. Rev. B: Condens. Matter Mater. Phys. 48 (1993) 11685–11691.
[35] E.A. Owen, D. Madoc-Jones, Proc. Phys. Soc. Lond. 67 (1954) 459.
[36] C.K. Cheng, S.Y. Foo, A.A. Adesina, Catal. Commun. 12 (2010) 292–298.
[37] C.K. Cheng, S.Y. Foo, A.A. Adesina, Catal. Today 178 (2011) 25–33.
[38] T. Xiao, T. Suhartanto, A.P.E. York, J. Sloan, M.L.H. Green, Appl. Catal., A: Gen. 253 (2003) 225–235.
[39] M. Zorko, S. Novak, M. Gaberscek, J. Ceram. Proc. Res. 12 (2011) 654–659.
[40] K.M. Parida, A.C. Pradhan, J. Das, N. Sahu, Mater. Chem. Phys. 113 (2009) 244–248.
[41] G.K. Chuah, S. Jaenicke, T.H. Xu, Microporous Mesoporous Mater. 37 (2000) 345–353.
[42] L. Shi, G. Yang, K. Tao, Y. Yoneyama, Y. Tan, N. Tsubaki, Acc. Chem. Res. 46 (2013) 1838–1847.
[43] P. Stelmachowski, G. Maniak, J. Kaczmarczyk, F. Zasada, W. Piskorz, A. Kotarba, Z. Sojka, Appl. Catal., B: Environ. 146 (2014) 105–111.
[44] P. Ratnasamy, H. Knözinger, J. Catal. 54 (1978) 155–165.
[45] T. Onfroy, W.C. Li, F. Schüth, H. Knözinger, Top. Catal. 54 (2011) 390–397.
[46] M. Zayat, D. Levy, Chem. Mater. 12 (2000) 2763–2769.
[47] U.L. Stangar, B. Orel, M.J. Krajnc, J. Sol-Gel Sci. Tech. 26 (2003) 771–775.
[48] H.S.C. O'Neill, Eur. J. Mineral. 6 (1994) 603–609.
[49] A. Natasuka, Y. Ikda, Y. Yamasaki, N. Nakayama, T. Mizota, Solid State Commun. 128 (2003) 85–90.
[50] Z. Liu, Y. Chen, J. Catal. 177 (1998) 314–324.
[51] R. Prihod'ko, E.J.M. Hensen, M. Sychev, I. Stolyarova, T.E. Shubina, I. Astrelin, R.A. van Santen, Microporous Mesoporous Mater. 69 (2004) 49–63.
[52] A. Davidson, J.F. Tempere, M. Che, H. Roulet, G. Dufour, J. Phys. Chem. 100 (1996) 4919–4929.
[53] G.R. Rao, H.R. Sahu, Proc. Nat. Acad. Sci. India Sect. A: Chem. Sci. 113 (2001) 651–658.
[54] M. Amimoto, M. Haneda, M. Ozawa, J. Phys.: Conf. Ser. 379 (2012) 012018.
[55] J. Lei, X.-H. Lu, J.-L. Zhang, X.-L. Wei, D. Zhou, Q.-H. Xia, Indian J. Chem. 52A (2013) 709–716.
[56] M.S. Aw, I.G. Osojnik Črnivec, P. Djinović, A. Pintar, Int. J. Hydrogen Energy 39 (2014) 12636–12647.
[57] I.G. Osojnik Črnivec, P. Djinović, B. Erjavec, A. Pintar, Chem. Eng. J. 207–208 (2012) 299–307.
[58] B. Liu, W. Ren, L. Gao, S. Li, S. Pei, C. Liu, C. Jiang, H.-M. Cheng, J. Am. Chem. Soc. 131 (2009) 2082–2083.
[59] M. Fernandez-Garcia, A. Martinez-Arias, A. Iglesias-Juez, C. Belver, A.B. Hungria, J.C. Conesa, J. Soria, J. Catal. 194 (2000) 385–392.
[60] M.M. Kamble, V.S. Waman, A.H. Mayabadi, S.S. Ghosh, B.B. Gabhale, S.R. Rondiya, A.V. Rokade, S.S. Khadtare, V.G. Sathe, T. Shripathi, H.M. Pathan, S.W. Gosavi, S.R. Jadkar, J. Coat. (2014) (Article ID 905903, 11 pages).
[61] R.L. Frost, M.L. Weier, P.A. Williams, P. Leverett, J. Theo Kloprogge, J. Raman Spectrosc. 38 (2007) 574–583.
[62] S. Reich, C. Thomsen, J. Maultzsch, Carbon Nanotubes: Basic Concepts and Physical Properties, first ed., Wiley-VCH, Weinheim, 2004.
[63] K. Takanabe, K. Nagaoka, K. Nariai, K.-I. Aika, J. Catal. 232 (2005) 268–275.
[64] L. Österlund, A.W. Grant, B. Kasemo, in: U. Heiz, U. Landman (Eds.), Nanocatalysis, Springer-Verlag, Berlin Heidelberg, 2007, p. 331.
[65] A. Al-Ubaid, E.E. Wolf, Appl. Catal., A: Gen. 40 (1988) 73–85.
[66] A. Trovarelli, Catal. Rev. Sci. Eng. 38 (1996) 439–520.
[67] C.L. Frewin, C. Locke, S.E. Saddow, E.J. Weeber, in: S.E. Saddow (Ed.), Silicon Carbide Biotechnology, Elsevier Sci. Ltd., UK, 2012, pp. 235–236.
[68] J. Guo, H. Lou, H. Zhao, D. Chai, X. Zheng, Appl. Catal., A: Gen. 273 (2004) 75–82.